Radial Tully–Fisher relation and the local variance of Hubble parameter

Balakrishna Haridasu, Paolo Salucci, Gauri Sharma

Monthly Notices of the ROYAL ASTRONOMICAL SOCIETY

MNRAS **532,** 2234–2247 (2024) https://doi.org/10.1093/mnras/stae1467
Advance Access publication 2024 June 12

Radial Tully–Fisher relation and the local variance of Hubble parameter

Balakrishna S. Haridasu [1,2,3]★ Paolo Salucci[1,2,3] and Gauri Sharma [1,2,3,4,5,6]

[1]*SISSA-International School for Advanced Studies, Via Bonomea 265, I-34136 Trieste, Italy*
[2]*INFN, Sezione di Trieste, Via Valerio 2, I-34127 Trieste, Italy*
[3]*IFPU, Institute for Fundamental Physics of the Universe, via Beirut 2, I-34151 Trieste, Italy*
[4]*Department of Physics and Astronomy, University of the Western Cape, Cape Town 7535, South Africa*
[5]*University of Strasbourg, CNRS UMR 7550, Observatoire astronomique de Strasbourg, F-67000 Strasbourg, France*
[6]*University of Strasbourg Institute for Advanced Study, 5 allée du Général Rouvillois, F-67083 Strasbourg, France*

Accepted 2024 June 10. Received 2024 June 3; in original form 2024 March 28

ABSTRACT

Utilizing the well-established radial Tully–Fisher (RTF) relation observed in a 'large' (843) sample of local galaxies, we report the maximum allowed variance in the Hubble parameter, H_0. We estimate the total intrinsic scatter in the magnitude of the RTF relation(s) implementing a cosmological model-independent cosmographic expansion. We find that the maximum allowed local 'radial' variation in our baseline analysis, using four RTF relations in the galaxy sample is $\Delta H_0/H_0 \lesssim 3$ per cent at a 95 per cent C.L. significance, which is implied form a constraint of $\Delta H_0/H_0 = 0.54^{+1.32}_{-1.37}$ per cent estimated at $D_{\rm L} \sim 10$ [Mpc]. Using only one 'best-constrained' radial bin, we report a conservative 95 per cent C.L. limit of $\Delta H_0/H_0 \lesssim 4$ per cent. Through our estimate of maximum variation, we propose a novel method to validate several late-time/local modifications put forth to alleviate the H_0 tension. We find that within the range of the current galaxy sample redshift distribution $10\,[\rm Mpc] \leq D_{\rm L} \leq 140\,[\rm Mpc]$, it is highly unlikely to obtain a variation of $\Delta H_0/H_0 \sim 9$ per cent, necessary to alleviate the H_0-tension. However, we also elaborate on the possible alternative inferences when the innermost radial bin is included in the analysis. Alongside the primary analysis of fitting the individual RTF relations independently, we propose and perform a joint analysis of the RTF relations useful to create a pseudo-standardizable sample of galaxies. We also test for the spatial variation of H_0, finding that the current samples' galaxies distributed only in the Southern hemisphere support the null hypothesis of isotropy within the allowed noise levels.

Key words: galaxies: distances and redshifts – cosmological parameters – dark matter.

1 INTRODUCTION

To determine the value of the 'Hubble Parameter': $H(z)$ at different redshifts and in particular at present (H_0) has become one of the most important and telling cosmological measurements. The well-established and increasingly prominent H_0-tension (Verde, Treu & Riess 2019; Di Valentino et al. 2021) has paved the way to speculate several modifications to the concordance model of cosmology. At present, the significance of this discrepancy between the local model-independent Cepheid calibration-based supernovae yield $H_0 = 73.04 \pm 1.04\,{\rm km\,s^{-1}\,Mpc^{-1}}$ (Riess et al. 2021) and the cosmic microwave background (CMB) based model-dependent (ΛCDM) indirect estimate $H_0 = 67.66 \pm 0.49\,{\rm km\,s^{-1}\,Mpc^{-1}}$ from the improved PR4 analysis in Tristram et al. (2024) is about $\sim 5\sigma$. In addition, the latter CMB estimate is corroborated by the Baryon Acoustic Oscillation data (Zhao et al. 2019; du Mas des Bourboux et al. 2020; Alam et al. 2021), providing $H_0 = 67.81 \pm 0.38\,{\rm km\,s^{-1}\,Mpc^{-1}}$, which only increases the significance of the said tension. A more recent claim for a 8.2σ tension was presented in Riess et al. (2024), addressing the cepheid crowding and their power-luminosity relation using *JWST* observations. Several reviews and discussions now provide a very good overview of the state of the tension (Riess 2019; Efstathiou 2020; Knox & Millea 2020; Freedman 2021; Schöneberg et al. 2022; Shah, Lemos & Lahav 2021; Abdalla et al. 2022; Perivolaropoulos & Skara 2022; Hu & Wang 2023; Verde, Schöneberg & Gil-Marín 2023; Akarsu et al. 2024). Also, other local calibration techniques and measurements either provide a similar disagreement with the CMB estimate or at least do not yield immediate resolutions (Bonvin et al. 2017; Chen et al. 2019; Freedman et al. 2019; Huang et al. 2020; Jee et al. 2019; Yuan et al. 2019; de Jaeger et al. 2020; Pesce et al. 2020; Schombert, McGaugh & Lelli 2020; Shajib et al. 2020; Wong et al. 2020; Blakeslee et al. 2021).

To resolve long-standing Hubble tension, several approaches have been proposed and explored ranging from modifications to early-Universe physics (Karwal & Kamionkowski 2016; Zhao et al. 2017; Kreisch, Cyr-Racine & Doré 2020; Jedamzik, Pogosian & Zhao 2021; Poulin, Smith & Bartlett 2021; Roy Choudhury, Hannestad & Tram 2021; Niedermann & Sloth 2021a, b; de la Macorra, Almaraz & Garrido 2022) to late-time/intermediate redshift physics (Solà, Gómez-Valent & de Cruz Pérez 2017; Khosravi et al. 2019; Tutusaus, Lamine & Blanchard 2019; Vattis, Koushiappas & Loeb 2019; Akarsu et al. 2020; Blinov, Keith & Hooper 2020; Haridasu & Viel 2020; Anchordoqui 2021; Akarsu et al. 2023; Lapi et al. 2023; Nygaard et al. 2023; Tutusaus, Kunz & Favre 2023; Adil et al.

★ E-mail: sharidas@sissa.it

2024), local Universe (Keenan, Barger & Cowie 2013; Whitbourn & Shanks 2014; Hoscheit & Barger 2018; Colgáin, Van Putten & Yavartanoo 2019; Kenworthy, Scolnic & Riess 2019; Luković et al. 2019; Shanks, Hogarth & Metcalfe 2019; Cai et al. 2020; Alestas, Kazantzidis & Perivolaropoulos 2021; Castello, Högås & Mörtsell 2022), leading to extended discussions and suggestions (Addison et al. 2018; Poulin 2020; Vagnozzi 2020; Bernal et al. 2021; Dainotti et al. 2021; Haridasu, Viel & Vittorio 2021; Krishnan et al. 2021; Dainotti et al. 2022; Cao & Ratra 2023; Dainotti et al. 2023; Lee et al. 2023; Lenart et al. 2023; Silva 2023; Vagnozzi 2023; Bargiacchi et al. 2023a; Bargiacchi, Dainotti & Capozziello 2023b; Gómez-Valent et al. 2024). Alongside modifications to the physics of the Universe, possibilities that tension can arise due to systematics have been explored many times (e.g. Mortsell et al. 2021, 2022; Wojtak & Hjorth 2022; Wojtak, Hjorth & Hjortlund 2023; Wojtak & Hjorth 2024). Several techniques to study the possible resolutions of the Hubble tension under the least possible cosmological assumptions have also driven the need for model-independent techniques that have substantial significance in recent times, for example, (Gómez-Valent 2018; Haridasu et al. 2018; Lemos et al. 2019; Liao et al. 2020; Lyu et al. 2020; Pandey, Raveri & Jain 2020; Du et al. 2023; Liu, Yu & Wu 2023; Qi et al. 2023; Li & Liao 2024, and references therein).

In this context, Kourkchi et al. (2020) have utilized the well-known Tully–Fisher relation (Tully & Fisher 1977; Tully 2023) to estimate the local expansion rate, which has been consistent and at times providing even larger value of H_0 with respect to the SH0ES estimate using SNe observables. Similarly, Kourkchi et al. (2022) implement the Baryonic Tully–Fisher (McGaugh et al. 2000; McGaugh 2005) relation assessing the same. These approaches have the advantage of possessing a clear physical justification (please see Salucci, Frenk & Persic 1993; Salucci 2019) and essentially highlight the necessity of alternate local estimations of H_0 aiding immensely in the discussion on H_0-tension and providing robust support to the Chepehid-SNe-based local determination of the same. For a recent discussion, see also Tully (2023). Along these lines, we intend to introduce the possibility of assessing the same using the radial Tully–Fisher (RTF) relation for the first time. The RTF relation has been well established in Yegorova & Salucci (2007), following the discovery of a strong global relationship between the rotation velocities and the absolute magnitudes ($M_{\rm I}$) of the ∼800 nearby galaxies (Persic, Salucci & Stel 1996; Salucci 2019, and references therein). The RTF relation indicates that there exist independent RTF-like relations at different galactocentric radii within spiral galaxies. In the current work, we take advantage of the RTF relation to obtain limits in the allowed variation of the Hubble rate within the local Universe $z < 0.035$, more precisely at the edge of the 'Hubble-Flow'.

Several local ($z < 0.1$) and ultra-local ($z < 0.01$) (Desmond, Jain & Sakstein 2019; Benevento, Hu & Raveri 2020; Desmond & Sakstein 2020; Alestas et al. 2021; Marra & Perivolaropoulos 2021; Banerjee, Petronikolou & N. Saridakis 2023; Högås & Mörtsell 2023) physical resolutions and possible variations in the standardization of SNe (Alestas et al. 2022; Benisty 2023; Camarena & Marra 2023; Perivolaropoulos & Skara 2023; Ruchika et al. 2024), have also been suggested to alleviate the H_0-tension, essentially relying on the fast transitions of physics in addition to the local void (Keenan et al. 2013; Whitbourn & Shanks 2014; Hoscheit & Barger 2018) and extremely local ($z < 0.015$) sharp transition of the dark energy equation of state in Camarena & Marra (2019) etc. We anticipate the ability of the RTF relation to constrain proposed local modifications to the cosmological scenario by estimating the allowed variance in the local estimation of the Hubble parameter. We begin by reanalysing the RTF relations presented in Persic et al. (1996) (here onwards PSS95) and Yegorova & Salucci (2007) (here onwards YS07) using improved Bayesian techniques. Given the nature of the empirical relations, we also propose a methodology for improving the RTF relations by introducing a joint analysis to constrain the relations simultaneously, modelling a covariance among the individual relations.

The organization of the paper is as follows: In Section 2, after a brief introduction to the RTF relation, we present the data utilized in the current work. The cosmographic methodology and fitting of the RTF relations are described in Section 3. Finally, in Section 4, we present the results with an extended discussion.

2 RADIAL TULLY–FISHER RELATION

Adopting $R_{\rm opt}$, the radius encompassing 83 per cent of the total light of a Spiral Galaxy, as the reference size of its stellar disc, the RTF relation is a family of TF-like relations observed in disc systems between the galaxy absolute magnitude in a certain j band (e.g. $M_{\rm I}$, the infrared band) and the rotational velocity $V(R/R_{\rm opt})$ measured at fixed normalized radii $R/R_{\rm opt}$. These relations have been well established in YS07 with the help of the large sample of galaxies with good quality RCs from PSS95 and that of two additional samples with 86 and 81 high-quality rotational curves (RCs) presented in Courteau (1997) and Vogt et al. (2004). In Fontaine et al. (2018), the RTF relationships have been established for a sample of 36 dwarf spirals and irregulars.

The RTF relations, for a given magnitude M_j, are represented by a class of linear models,

$$M_j = a_n \times \log_{10}(V_n) + b_n, \tag{1}$$

where the subscript n tags the radial bins in which the RTF is established. These bins are centred at the radii R_n, defined in terms of fractions of the optical radii. For the PSS95 sample that we use in this work: $R_n \equiv n/5R_{\rm opt}$ and the bin width is $1/5R_{\rm opt}$. Noticeably, the RTF has also emerged by adopting a smaller bin size, e.g. $1/15R_{\rm opt}$, as in YS07 for the Courteau (1997) and Vogt et al. (2004) samples of high-resolution RCs.

For the galaxies of the current sample, $V_n \equiv V(R_n)$ is the average value of the velocity data in each $n^{\rm th}$ bin, a_n and b_n are the slope and the intercept of the linear RTF relations found for the data belonging to the $n^{\rm th}$ bin.[1] Let us notice that in the constant b_n, we can incorporate the term $M_j(\infty) - M_j(R_n)$, which at a fixed n is equal in all galaxies, so that the L.H.S of equation (1) can be interpreted as the aperture j-magnitude at the radius R_n, a quantity related to the mass in stars inside such radius.

It is worth demonstrating here that the RTF relationship with the features described above has a strong physical background as the originating TF one: it is a direct consequence of the fact that spiral galaxies are rotationally supported; their circular velocities, at a radius R balance the gravitational attraction of the galaxy mass inside this radius R. Remarkably, in spirals the mass distribution has universal features (see Salucci (2019)) and it includes 1) a Freeman stellar disc of mass $M_{\rm D}$ and length-scale $R_{\rm D}(M_{\rm I})$, whose contribution to the circular velocity $V(R)$ can be written as $V_{\rm d}(R/R_{\rm D}; M_{\rm D})$ with the disc mass $M_{\rm D}$ as a free parameter of the mass model. 2) a cored dark matter halo whose contribution to $V(R)$ can be written

[1] Since the surface luminosity density of the stellar disc $I(R)$ is very similar in all spirals and it is represented by the well-known Freeman profile: $I(R) \propto {\rm e}^{-R/R_{\rm D}}$, the length-scale $R_{\rm opt} = 3.2R_{\rm D}$ describes the distribution of luminous matter for every spiral galaxy in the same consistent way.

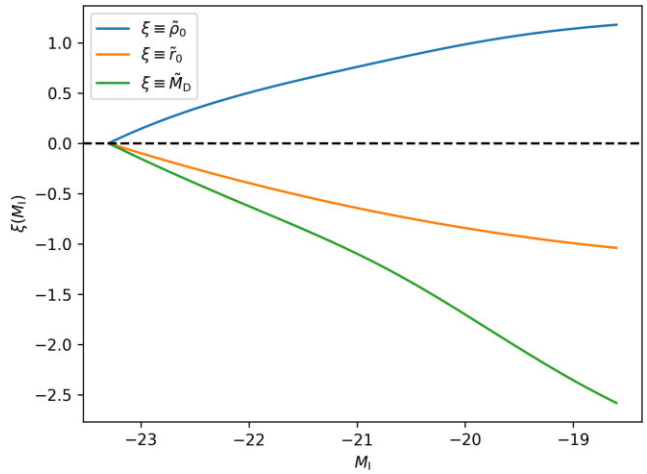

Figure 1. The parameters of the mass model of Spiral galaxies plotted as functions of the infrared Magnitude M_I. $\tilde{\rho}_0(M_I) = \rho_0(M_I)/(1.2 \times 10^{-25}\,\mathrm{g\,cm^{-3}})$ (blue), $\tilde{r}_0(M_I) = r_0(M_I)/(54\,\mathrm{kpc})$ (orange), $\tilde{M}_D(M_I) = M_D(M_I)/(4 \times 10^{11}\,\mathrm{M_\odot})$ (green).

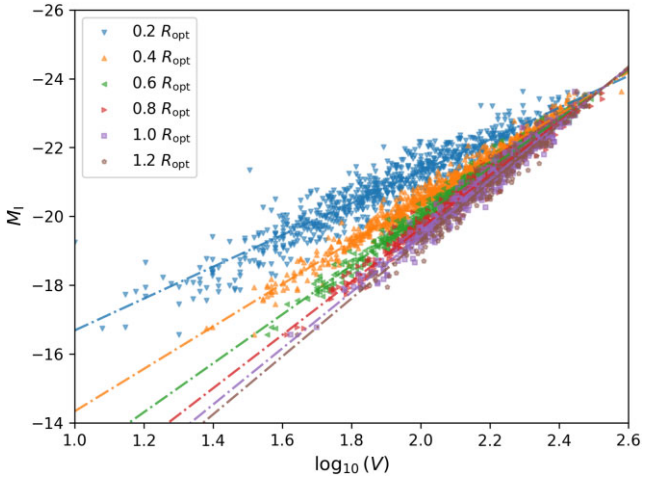

Figure 2. Scatter corresponding to the RTF relations in the six bins of R_{opt} taken from PSS95 and the linear best-fits obtained from our joint analysis described in Section 3.2, assuming $H_0 = 70\,\mathrm{km\,s^{-1}\,Mpc^{-1}}$.

as $V_h(R; \rho_0, r_0)$ (Salucci (2008)), with the central density ρ_0 and the core radius r_0 also as free parameters of the mass model. The resulting circular velocity model:

$$V_{\rm model}(R) = \left[V_d^2(R/R_D; M_D) + V_h^2(R; \rho_0, r_0)\right]^{1/2} \quad (2)$$

successfully fits the circular velocities $V(R)$ of the entire family of Spiral galaxies (PSS95; Salucci & Burkert (2000); Karukes & Salucci (2017); Salucci (2019)) provided that the above three free structural parameters become specific functions of the galaxy's infrared magnitude M_I

$$M_D(M_I); \quad r_0(M_I); \quad \rho_0(M_I), \quad (3)$$

shown in Fig. 1 and given in PSS95 (see also Salucci & Burkert (2000)). By inserting the equation (3) into equation (2), one obtains that the latter becomes equivalent to the equation (1) with the values of parameters given by Table 1 (see YS07 for the more details).

A further prediction of the physical origin of the RTF relationship is that in the innermost bin (i.e. for $n = 1$) the relation should show a scatter sensibly larger than in the outer bins (i.e. for $2 \leq n \leq 5$). This is due to the presence, in a good fraction of the objects of the sample, of a central stellar bulge that provides an important contribution to the mass enclosed in the innermost radius. The mass of this spheroid has a trend with that of the stellar disc, so that, the RTF continues to exist also for $n = 1$, but with a scatter larger than those at farther radii, not affected by the central bulge mass (see YS07). Let us also point out that, according to the above velocity model and directly supported by RCs data, we have

$$V_{\rm model}(n/5\,R_{\rm opt}, -23.) \simeq 10^{2.5}\,\mathrm{km\,s^{-1}} \quad (4)$$

for $1 \leq n \leq 5$. Thus the RTF relationship, that will be used here as a distance indicator, reflects the condition of the centrifugal equilibrium of a stellar disc embedded in a dark halo.

As shown in Yegorova & Salucci (2007) and Di Paolo, Salucci & Fontaine (2019), the kinematics of inner regions ($R < 1/3 R_D$) in disc galaxies is strongly affected by the random presence of a central bulge with half-light radius of (1/5–1/3) R_D and a mass (1/10–1/4) that of the stellar disc. The introduction of this additional stellar component increases the success of the adopted mass model (bulge, disc, dark halo) in reproducing the features of the RTF, the URC (Persic et al. 1996) and also the individual RCs of disc systems, especially for their largest masses. However, this result implies that the circular velocities in the $n = 1$ ($0.2\,R_{opt}$) bin are affected randomly by the presence of a central bulge whose structural properties have a less stringent dependence on the galaxy luminosity but with a larger scatter, as it is well known by complete photometric studies. This scenario with a fair correlation and large scatter between the structural properties of the bulge and mass components does not destroy the RTF relation for the $n = 1$ bin but makes its slope shallow and its scatter larger (Figs 2 and 5). To use the RTF of this bin in an unbiased way we should have a precise indicator for individual galaxies' Bulge mass and of its half-light radius. More importantly, second bin onwards

Table 1. We show the posteriors, including the 68 % C.L. limits for the linear regression parameters, performed for each of the radial bins shown in Fig. 2. The first column is the radial bins and the next three columns present the results obtained by fitting the RTFs individually. In columns 4 and 5 we show the results obtained in the joint analysis. In the last column, we show the number of data points utilized in the regression in each bin. All constraints reported here are obtained assuming $H_0 = 70$ km/s Mpc^{-1}.

				Joint		
R_n [R_{opt}]	b_n	a_n	σ_n^{int}	a_n	σ_n^{int}	N_D
0.2	-11.98 ± 0.11	-4.67 ± 0.06	0.402 ± 0.011	-4.62 ± 0.04	0.370 ± 0.012	749
0.4	-8.18 ± 0.07	-6.15 ± 0.03	0.191 ± 0.005	-6.16 ± 0.03	0.108 ± 0.010	793
0.6	-5.78 ± 0.06	-7.11 ± 0.03	0.148 ± 0.004	-7.11 ± 0.02	0.013 ± 0.009	799
0.8	-4.21 ± 0.09	-7.72 ± 0.04	0.173 ± 0.005	-7.76 ± 0.03	0.068 ± 0.016	663
1.0	-3.02 ± 0.15	-8.20 ± 0.07	0.214 ± 0.007	-8.18 ± 0.04	0.145 ± 0.012	454
1.2	-2.06 ± 0.26	-8.61 ± 0.12	0.262 ± 0.013	-8.44 ± 0.06	0.157 ± 0.004	231

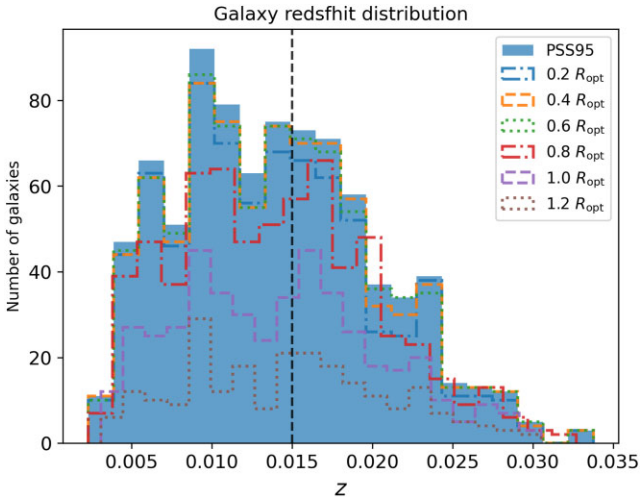

Figure 3. Redshift distribution of the PSS95 sample consisting of 489 galaxies below $z < 0.015$ and 384 galaxies from $z > 0.015$. We also show the number of galaxies contributing velocity data to each of the individual RTF relations as unfilled histograms.

the *random* presence of a central bulge does not affect the circular velocities. Let us also stress that the equally random effect of the presence of a central SMBH on the RTF is always negligible (see Salucci et al. 2000).

Data: In the current work, we utilize the same data set that has been used to work out the 'Universal rotational curve' in PSS95 and later analysed in YS07 to work out the RTF. The data set provides the magnitude of the galaxies in the 'I' band against the binned rotational velocity in each of the optical bins. In Fig. 3, we show the redshift distribution of the galaxies which range between $0.005 \leq z \leq 0.035$, incidentally centred around $z \sim 0.015$, similar to the lower limit of $z > 0.023$ usually taken to estimate the local value of H_0 in SH0ES analysis (Riess et al. 2016, 2018b), allowing the SNe to be in the 'Hubble flow'. We also show the number of galaxies contributing rotational velocities to each of the individual RTF relations, summing up to the total number of data points utilized in the current analysis. Notice that the peculiar motions of the galaxies in our sample, assumed to be 200 km s^{-1}, affect the determination of their redshift with an error, on average, of about ± 0.08 mag, i.e. a value smaller than the intrinsic scatter of the RTF relations, that amount to 0.12–0.25 mag; therefore, systematics that may arise in having not detailed these motions is small and likely washed out by the random uncertainty of the RTF relations. Moreover, in this work, the RTF distance indicator is used for tasks, whose complement does not require a good knowledge of the peculiar motions of galaxies.

In Fig. 2, we show the RTFs for the different optical radii, alongside the best-fit linear relations, elaborated in Section 4. The distribution of these galaxies in the sky is shown in the Fig. 4, which are a subset of those presented in the southern sky survey (Mathewson, Ford & Buchhorn 1992). Here, we show the distribution of the galaxies in Fig. 4, in the J2000 system in contrast to the B1950 as was originally presented in Mathewson et al. (1992).

In summary, the radial TF has been established in the process of investigating, in an innovative way (YS07), the mass distribution of spirals for the region inside their optical radii, essentially providing evidence for: i) the presence of a massive dark component, ii) the decrease of the DM/total matter fraction with increasing galaxy luminosity, iii) a very shallow halo density profile, and iv) the presence of a central bulge component. The role of the RTF thus far has therefore been primarily intended to study dark matter properties in galaxies (e.g. Salucci (2019)). However, given the recent Hubble Tension, this tight and physically motivated Tully–Fisher-like relationship, even using the 'original' data set can be a very efficient distance indicator. The improvement with respect to the TF is obvious: the latter uses one circular velocity at a reference radius per galaxy, while the RTF exploits the full RC rotation curve inside the same optical radius of each galaxy.

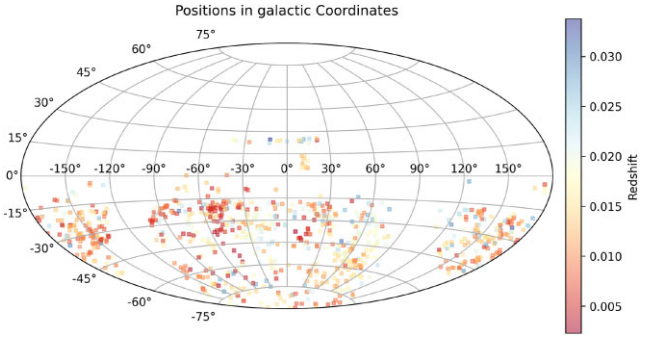

Figure 4. Distribution of the galaxies utilized in the current analysis. The vertical colour bar shows the redshift distribution of the galaxies.

3 METHOD

We adopt the linear models shown in equation (1) to perform regression to obtain the posteriors for each of the radial bins defined above in terms of the optical radius. In detail, first we perform a simple linear regression for each of the subsamples split into the six bins with centres located at each of the first six 0.2 multiples of R_{opt}, wherein all the data points are assumed to be independent and no correlation is assumed in the analysis. For consistency, after performing the initial regression, we exclude the data points that are more than 3σ confidence level away from the posterior regressed line to exclude the outliers. However, we also note that this exclusion of the outliers does not significantly affect the final inferences drawn from the analysis. The analysis requires three parameters for each of the RTF relations taking into account the slope, intercept, and intrinsic scatter $\{a_n, b_n, \sigma_n\}$, amounting to a total of 18 total parameters to fit the six optical bins considered in the current data set. Note that throughout the analysis, we assume and fix a fiducial value of $H_0 = 70\,\mathrm{km\,s^{-1}\,Mpc^{-1}}$ and $q_0 = -0.55$. Assuming a different value of H_0 within the current analysis with the simple cosmographic background presented in the next section, mainly gives rise to an overall shift of RTF relations with minor differences in the shape of the RTF relations. This remains a valid assumption given that there exists no significant empirical indication to go beyond the linear relations.

3.1 Cosmography

To utilize the given galaxy samples to estimate the maximum allowed variance in the Hubble parameter, we implement a simple cosmographic approach to model the luminosity distance as,

$$D_{\rm L}(z) = \frac{c}{H_0} \times \left[z + \frac{1}{2}(1 - q_0) z^2 \right], \tag{5}$$

where H_0 is the current expansion rate and q_0 is the deceleration parameter. The distance modulus can now be written as the difference

between the apparent magnitude and the absolute magnitude,

$$m_{\rm I} - M_{\rm I} = 25 + 5\log_{10}(D_{\rm L}(z)[{\rm Mpc}]), \quad (6)$$

wherein we utilize the recession velocity ($V_{\rm rec}$) of each of the galaxies to obtain the redshift $z = V_{\rm rec}/c$. Note that the above equation can further be approximated, taking only the first-order term in equation (5) into account,

$$m_{\rm I} - M_{\rm I} = 25 + 5\log_{10}(V_{\rm rec}/H_0). \quad (7)$$

From equation (7), we have that in a local ($z \ll 0.1$) sample of objects, each of them with well-measured $m_{\rm I}$ and $V_{\rm rec}$, if in the expansion of the Universe, the quantity $H(z)/H_0$ changes with redshift differently from how it does in the assumed standard ΛCDM scenario (or a simple cosmography): $H_{\Lambda{\rm CDM}}(z)/H_0$ ($\simeq 1 + {\rm O}(10^{-3})$ for the objects in our sample), which introduces the presence of an extra *systematical* term $\delta M_{\rm I} = -5\ \log_{10}[H(z)/H_{\Lambda{\rm CDM}}(z)]$ in the determination of the absolute magnitudes $M_{\rm I}$ from the observed $m_{\rm I}$ and $V_{\rm rec}$. It is worth to remark that the peculiar velocity ($V_{\rm p}$) of a galaxy with respect to the Hubble flow $V_{\rm p} \sim 200$–$300\,{\rm km\,s^{-1}}$ introduces a *random* error on $M_{\rm I}$ of order $\sim 5\log_{10}[(V_{\rm p} + V_{\rm rec})/V_{\rm rec}]$ which, within the context of present work, gets statistically damped/averaged out by the large number of objects in the sample.

Finally, given the assumed cosmography to obtain the absolute magnitude of the data points and the posteriors of linear regression models obtained through the fitting relation equation (1), we construct the residuals of the absolute magnitude as a function of the redshift. The redshift of the galaxies is consistently obtained utilizing the recession velocity of the galaxies, as described earlier. Also, one could equivalently present the same in terms of the luminosity distance of the galaxies instead of redshift, which we present as the final result (elaborated in Section 4).

3.2 Joint analysis

The methodology described so far follows YS07 and constrains each of the RTF relations individually. While we utilize the same as a first step, in this work, we also introduce a method to perform joint analysis and simultaneously constrain the RTF relations. As can be seen in Fig. 2 and also in Fig. 2of YS07, all the individual RTF relations at each optical bin converge at a 'pivot' that remains to be a fixed point depending only on the value of H_0 assumed in the conversion of the observed apparent magnitudes to the absolute magnitude $M_{\rm I}$ through equation (5) and the distance modulus expression. As shown in Section 2, we remind that the mass model of spiral galaxies at all radii is observationally unrelated to the RTF, implying the existence of this pivot quantity.

This, in turn, modifies the individual RFT description in equation (1) with a pivot as,

$$M_j - M_{\rm I}^{\rm Pivot} = a_n \times (\log_{10}(V_n) - \log_{10}(V^{\rm Pivot})), \quad (8)$$

where the pivot is given by $\left\{M_{\rm I}^{\rm Pivot}, \log_{10}(V^{\rm Pivot})\right\}$ and the corresponding slopes a_n of the individual relations. In contrast to the total of 18 parameters describing the six independent relations, within the joint analysis set-up, we have 14 parameters: 12 describing the slopes and intrinsic scatter of the six relations, and two fixing the pivot.

3.3 Likelihood

The likelihood of the individual linear regression analysis within each of the radial bins n can be written as,

$$-2\log(\mathcal{L}) = \sum^{N^n_{\rm gal}} \left[\frac{\left(M_{\rm I}^{\rm obs} - M_{\rm I}^{\rm theo}(V_n)\right)^2}{\sigma_n^2} + \log\left(2\pi\sigma_n^2\right) \right], \quad (9)$$

where the $M_{\rm I}^{\rm obs}$ is constructed using equation (6), while the $M_{\rm I}^{\rm theo}(V_n)$ assume the form in equation (1), with the free parameters $\Theta \equiv \{a_n, b_n\}$, and σ_n is a free parameter assessing the intrinsic scatter of the data. Here, $N^n_{\rm gal}$ is the number of galaxies with rotational curve velocities in $n^{\rm th}$ radial bin. Similarly, the likelihood for the joint analysis is written as,

$$-2\log(\mathcal{L}) = \sum^{n}\sum^{N^n_{\rm gal}} \left[\frac{(M_{\rm I}^{\rm obs} - M_{\rm I}^{\rm theo}(V_n))^2}{\sigma_n^2} + \log(2\pi\sigma_n^2) \right], \quad (10)$$

wherein a summation over the radial bins n is included and the $M_{\rm I}^{\rm theo}(V_n)$ is given by equation (8), with free parameters $\Theta \equiv \{M_{\rm I}^{\rm Pivot}, \log_{10}(V^{\rm Pivot}), \mathbf{a_n}\}$ amounting to a total of 14 parameters as described earlier. Note that one could include an additional parameter τ as a penalty term $\log(\tau + \sigma_n^2)$ to the total likelihood. This would describe a degeneracy/covariance between the six RTF relations, to be more conservative and validate the utility of the magnitude used in RTF relation at each optical bin. In other words, the parameter τ takes into account the variability between the individual RTF relations, enforcing a covariance amongst them. However, note that this does not curtail the use of individual RTF relations to asseses the Hubble variance, but aids an opportunity to construct a 'standardizable' sample of galaxies that follow a scaling relation, and can be utilized for additional distance ladder analysis, which we intend to perform as an independent full-fledged analysis. As we shall elaborate later in Section 4.3, we do not find strong correlations between individual radial bins, and therefore we leave this assessment to a future analysis.

To perform the fully Bayesian analysis, we utilize the publicly available `emcee`[2] package (Foreman-Mackey et al. 2013), implementing an affine-invariant ensemble sampler. We analyse the generated MCMC samples using `corner` and/or `GetDist`[3] Lewis (2019) packages.

3.4 Isotropy of the local Universe

Given the availability of the galaxy positions Mathewson et al. (1992), we also estimate the isotropy and the subsequent variance in the sky of the current sample. Note that the current sample only covers the southern sky and is not an isotropic survey allowing us to assess the overall isotropy being biased on large scales. Therefore, we estimate the overall noise level that would be expected in an isotropic universe, utilizing the bootstrapping methodology presented in Soltis et al. (2019) (see also Tarnopolski 2017; Andrade et al. 2018, 2019, for similar approaches). In this method, the positions of the galaxies are permuted amongst themselves, essentially rearranging under the assumption that in an isotropic universe, the galaxies could have been observed in any of the given positions within the sky coverage of the survey. In Soltis et al. (2019), the residuals of the supernovae magnitudes within the MCMC fitting are utilized as the indicators for the noise levels. Similarly, we utilize

$$r_{\rm i} = \frac{M_{\rm I,i}^{\rm theory} - M_{\rm I,i}^{\rm data}}{\sigma_{M_{\rm I,i}^{\rm data}}} \quad (11)$$

as the indicators for the same, where i iterates over the number of galaxies. The assumption of these residuals as an indicator is valid as we do not intend to estimate the actual isotropy itself but rather the noise level present within the distribution of the galaxies and contrast against the observed positions of the galaxies. Using these residuals in the sky, we estimate the clustering of the galaxies by estimating

[2] http://dfm.io/emcee/current/
[3] https://getdist.readthedocs.io/

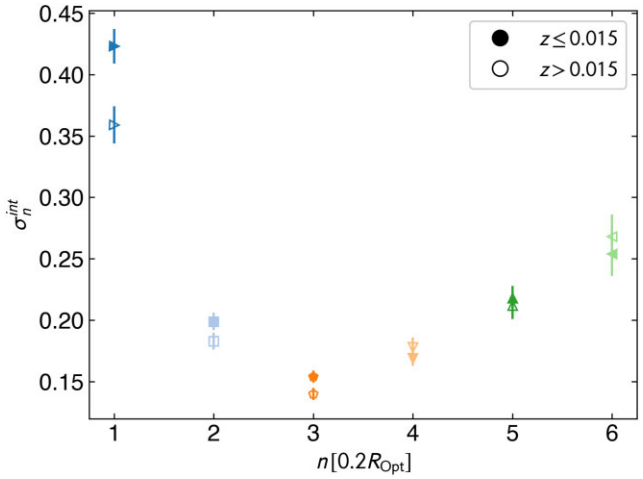

Figure 5. The intrinsic scatter and the 1σ error, within each of the radial bins, however, split at redshift $z \sim 0.015$ to assess the variation in the different redshift bins.

the angular power spectrum C_l, the range of which depends on the assumption of the NSIDE[4] of the constructed maps. In this analysis, we present our results for NSIDE =16, while we validate that a different assumption does not change our inference substantially. For each of the galaxies, we take the total residual obtained from all the available optical bins and then an average value of these residuals for all the galaxies falling within each pixel of the map. We perform 1000 bootstrap steps for every set of the model parameters within the MCMC chain that are iterated 1000 times, yielding a total of a million steps taking into account uncertainty in the RTF relations. It is important to note that the linear regression of the RTF relations described in the earlier sections is performed assuming no uncertainty ($\sigma_{M_{\rm I,i}^{\rm data}} = 0$)[5] on the $M_{\rm I,i}^{\rm data}$. However, in estimating the noise level associated with the statistical isotropy, we assume the reasonable conservative value of $\sigma_{M_{\rm I,i}^{\rm data}} = 0.075$ (Mathewson et al. 1992) for the photometric measurements errors.

4 RESULTS AND DISCUSSION

We begin by re-analysing the PSS95 sample containing six different radial bins ($R_{\rm opt}$). The results obtained for the fitting of the individual RTFs are summarized in Table 1 for completeness, and are consistent in comparison to those presented in YS07 (see table A1 therein). In the current Bayesian formalism, the mean values of the scatter are mildly larger along with associated uncertainty. Following this to assess the redshift variation, as a preliminary step, we split the galaxy sample into two redshift bins performing the linear regression in each of the radial optical bins. In Fig. 5, we show the intrinsic scatter as obtained for each of the radial bins when the regression is performed with only samples $z \leq 0.015$ and $z \geq 0.015$ considered independently. We find a very good consistency between the intrinsic scatter estimated for the galaxies with the redshift cut, which asserts that a redshift-dependent analysis would not be biased due to the variation in the galaxy data set over redshift. This allows us to estimate the variance of the Hubble parameter as a function of redshift and, consequently luminosity distance. For the innermost optical bin 0.2 $R_{\rm opt}$, we find the intrinsic scatter is mildly larger for $z < 0.015$, however consistent within 2σ. Given the large intrinsic scatter in this bin, mostly due to the random presence of a not-negligible compact bulge component in our galaxies, it is difficult to estimate the rotational velocity very accurately along the lines of the bulge-free equation (2). Therefore, we exclude this bin in our baseline analysis when estimating the overall variance.[6] We also exclude the outermost bin, owing to the low sample density having only ∼230 data points, and the fact that the accuracy in measuring the rotational velocity from the H_α line is low at the outskirts of the spiral galaxies. Nevertheless, we retain the advantage of utilizing four independent radial bins to estimate the overall scatter. From here onwards, we remain with four optical bins as our 'baseline' data set to present our main results to evaluate the cosmological variance of the Hubble parameter. However, we do comment on the implications of utilizing these two bins as they present interesting scenarios in assessing the Hubble variance. The 0.6 $R_{\rm opt}$ bin having the least scatter.[7] and being best constrained RTF, is a conservative estimate to which we compare the joint constraint in our analysis.

Having the Tully–Fisher relation fitted in each of the bins, and establishing that the data set is suitable for the assessment of redshift variation, we now evaluate the residual of the absolute magnitude, w.r.t the fitted linear regression. We conservatively anticipate the intrinsic scatter and hence the absolute residual, $\Delta M_{\rm I}$ to account for cosmological variation that can be converted to the variance in the expansion rate as given by equation (12), also considering the uncertainty of the RTF relations.[8] Note that we also exclude the galaxies that are more than 3σ away from the residuals deeming them to be outliers.[9] Following equation (7), we now translate the average dispersion in the residual of RTF relation as the maximum possible variance (see Section A) in the value of H_0 as,

$$\overline{\frac{\Delta H_0}{H_0}}(z) = \frac{\ln 10}{5}\overline{\Delta M}(z), \tag{12}$$

which is now recast as the redshift evolution of the allowed fractional variation in the Hubble parameter as shown in Fig. 6, by binning the residuals appropriately in luminosity distance ($D_{\rm L}$). In this figure, we show the mean of the residuals for the best-fit RTF relations and the uncertainity on the same, estimated as the standard error. We present the residuals in all the radial bins while assessing the corresponding cosmological distance ($D_{\rm L}$) using equation (7), assuming that the redshift is given by the recession velocity ($V_{\rm rec}$) as $z = V_{\rm rec}/c$. We then compute the average variation of the $\Delta M_{\rm I}$ in each of the redshift/distance bins split accordingly. Needless to say, the difference in the number of data points (galaxies) in each bin is reflected in the uncertainty estimated as standard error $\sigma_{\overline{\Delta {\rm H}_0/{\rm H}_0}} = \sigma_{\Delta {\rm H}_0/{\rm H}_0}/\sqrt{n_{\rm i}}$, where $n_{\rm i}$ is the number of data points (galaxies) in each redshift bin. As we have already mentioned,

[4]The NSIDE fixes the resolution of the maps.

[5]The anticipated intrinsic scatter of the RTF relations is much larger than error on the magnitudes of the galaxies, and the inclusion of $\sigma_{M_{\rm I,i}^{\rm data}}$ error would fall completely within the prior. For this reason, we remain with fitting the RTF relations to estimate the maximum scatter.

[6]The effect of the bulge in RTF is discussed in YS07.

[7]Also for the RTFs emerging in the Courteau (1997) and Vogt et al. (2004) samples.

[8]We validate that including the uncertainty of the RTF relation itself makes very little difference to our final estimates, since the intrinsic scatter much larger in comparison.

[9]We find only about 5–10 galaxies per radial bin to satisfy the outlier condition, which however could be an important assessment as the lower $D_{\rm L} < 20$ [Mpc] and $D_{\rm L} > 120$ [Mpc] distance bins with a low number of galaxies can get mildly affected. We also validate that this step does not make a significant difference to our final inference.

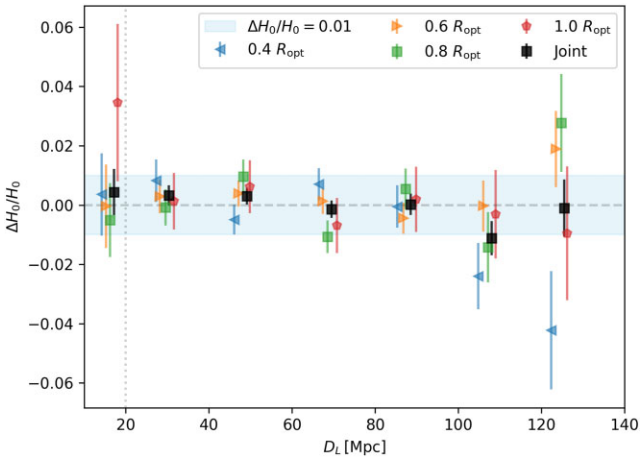

Figure 6. The variation in the Hubble parameter utilizing all five radial optical bins simultaneously. The data points have been slightly shifted in the x-axis for better visualization.

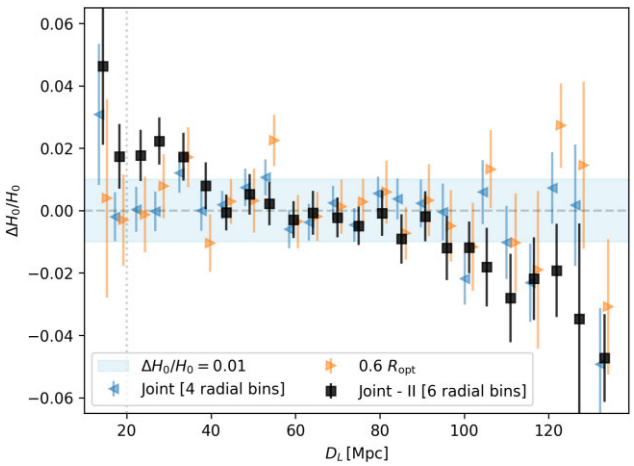

Figure 7. Same as Fig. 6 with different binning schemes and inclusion of the innermost radial 0.2 R_{opt} bin. Black data points show the results using the same binning as in Fig. 6.

each of the RTF relations fitted in the six optical bins can be considered independent relations with no correlations whatsoever. Therefore, in the joint analysis of all the radial bins $R_n[R_{opt}]$ considered, we follow the same procedure considering each velocity measurement in each radial bin as an independent data point. In Fig. 6, we show the variation in the residuals of absolute magnitudes of the galaxies, as a function of the luminosity distance, wherein we have binned the luminosity distance into linear bins of size $\Delta D_L = 20$ [Mpc].

As can be seen in Fig. 6, we find that there is no discernible redshift evolution of the Hubble variance, always consistent within ∼5 per cent, suggesting no variation in the current redshift range. We find that the joint constraint to sub percent precision always being consistent with $\Delta H_0/H_0 = 0$ within the $\sigma_{\overline{\Delta H_0/H_0}}$. For the 0.4 R_{opt}, we find the maximum variation to be ∼10 per cent comparing the data point at ∼120 Mpc with the innermost data point at ∼17 Mpc. Similarly, the 1.0 R_{opt} also shows a mild increase in the variance in the innermost distance bin. However, this trend is not immediately corroborated in the 0.6 R_{opt} and 0.8 R_{opt} radial bins, which are the better-constrained RTF relations showing no statistically significant trend. This is also reflected in the joint constraint shown as black data points in Fig. 6. Moreover, there seems to be a mild decrease in the values of $\Delta H_0/H_0$, especially around the $D_L = 100$ [Mpc] range; however, completely consistent within the $\sim 2\sigma$ C.L. for $\Delta H_0/H_0 = 0$.

We contrast our results for the uncertainty in the evolution of the Hubble parameter against the constraints obtained from the supernovae data sets in the local Universe. Although, the current galaxy data set utilized in this work only extends up to $D_L \sim 140$[Mpc], we confirm that within this range such an underdensity is not suggested by utilizing the RTF relation. This is in agreement with the earlier analysis in Camarena & Marra (2019), Kenworthy et al. (2019), Luković et al. (2019), Castello et al. (2022) using SNe data sets. An under density of size ∼300 [Mpc] (Hoscheit & Barger 2018) and a similar less significant local hole of ∼150 [Mpc] (Whitbourn & Shanks 2014; Shanks et al. 2019) were proposed as possibilities to alleviate the Hubble tension by modifying the current expansion rate measured by the local supernovae. To comment on which one would need to extend the current sample to a higher redshift range (Stone et al. 2022) (left for a future investigation). We note that the maximum variance estimated here in our binned analysis is comparable and is in complete agreement to that found in the SNe samples in Zhai & Percival (2022) where a $\Delta H_0 \sim \pm 1\,\mathrm{km\,s^{-1}\,Mpc^{-1}}$ is reported, using SNe extending into the Hubble-flow. Our galaxy data set here is better suited to study the local variance $z \leq 0.03$, which is lower than what is expected in the SNe samples. We find a very good agreement with the results therein within the overlapping range of $50\,\mathrm{Mpc} \leq D_L \leq 140\,\mathrm{Mpc}$.

Within the redshift range of the current data set, we find that local $z < 0.01$ sharp phantom transitions as proposed in Alestas et al. (2021) are less likely. Similarly, sharp transitions in the gravitational constant (G_N) local/ultra-local Universe (Marra & Perivolaropoulos 2021; Alestas et al. 2022; Benisty 2023; Camarena & Marra 2023; Perivolaropoulos & Skara 2023) and local modifications (Ruchika et al. 2024) have also been suggested as a possibility for the discrepancy in the locally measured H_0 and the value inferred from the CMB assuming model, which our results so far do not immediately suggest. In other words, we notice that in the current linear binning of distance, the innermost constraint obtained at $D_L \sim 17$ [Mpc] is completely consistent with no evolution of the $\Delta H_0/H_0$. This constraint is also consistent with the second bin centred at $D_L \sim 30$ [Mpc]. As can be seen in Fig. 6, our conservative inference using only the radial bin 0.6 R_{opt} is completely consistent with the joint constraint of the four considered so far. However, please refer also to the Sections 4.1 and Appendix B for mild yet alternate perspectives mostly arising due to different binning schemes and the inclusion of inner and outermost radial bins.

4.1 Inclusion of the innermost bin and alternate binning

In this section, we present the results as obtained when the innermost 0.2 R_{opt} and outer bins 1.2 R_{opt} are also included in the analysis. We also change the binning scheme of the distances to test for the validity of including the innermost bin while accommodating variations also on the closet and the farther-distance bins. In Fig. 7, the black data points show the joint constraint taking into account all the R_{opt} bins and increasing the number of distance bins in contrast to the earlier results in Fig. 6. As one can immediately notice the the joint constraints show a trend of increasing $\Delta H_0/H_0$ for lower distances. This change is completely driven by the 0.2 R_{opt} bin alone, while the outermost bin, having only 231 data points, makes minimal difference to joint constraints.

We show results for finer binning in distances with $\Delta D_{\rm L} \sim 5$ [Mpc] at the expense of precision in each bin to evaluate the overall shape of $\Delta H_0/H_0(z)$. We find that the $0.2\,R_{\rm opt}$ strongly influences the joint constraint, showing significant evidence for a possible cosmological signature for an increasing value of the Hubble parameter in the 'ultra-local' ($D_{\rm L} \lesssim 30$ [Mpc]) regime. Needless to say, to make this inference is heavily reliant on the binning scheme, as the closer distance bins tend to have very few galaxies providing the jump we notice therein. For instance, within the joint analysis of all the radial bins (black data points in Fig. 7), the first bin centred at $D_{\rm L} \sim 14.4$ [Mpc] and the last bin at $D_{\rm L} \sim 133.2$ [Mpc] contain merely five and three galaxies, respectively. In this case, the difference in the bins is $\Delta H_0/H_0 \sim 0.1$, which is about $\sim$10 per cent variation in the value of absolute H_0. Note that this level of variation difference could play a significant role in explaining the H_0-tension, which is $\sim$8 per cent difference between the local and the CMB estimates. We also show and validate that the $0.6\,R_{\rm opt}$ radial bin shows no such behaviour using the finer bins, with mildly increasing scatter of the mean at larger distances.

The initial consideration to leave this bin out of the joint analysis is because the central bulge in the spiral galaxies does not allow one to measure the rotational velocity accurately. Therefore, the validity of the redshift-dependent behaviour of $\Delta H_0/H_0$ we find in Fig. 7 is subject to confidence in the rotational velocities measured in the innermost regions of the spiral galaxies. In YS07, the authors provide a relationship (see eq.14 therein) between the slopes of the individual RTFs and the optical radii, indicating the validity of the RTFs also in the bulge of the galaxies. This is once again an empirical relation that is observed and fitted in the current galaxy sample, and it is also shown that this expectation is consistent when considering the two other galaxy samples they have tested. However, in a conservative approach, we keep to our four-bin analysis or equivalently, five bins including the outermost radial bin, not claiming significant evidence for a redshift evolution of $\Delta H_0/H_0$. This variation has to be validated in larger galaxy samples with better estimations of the central rotational velocities and would be untimely to claim a possible detection of local variation in H_0 using the current data set alone. We leave this for a future investigation using the PROBES (Stone et al. 2022) data set. However, it is interesting to note that the innermost bin carries significant statistics being able to sway the joint analysis using all six bins.

With the inclusion of the innermost optical bin, the mean values of $\Delta H_0/H_0$, inferred using only the four bins, increase by more than a 2σ significance. This can be inferred straightaway by comparing the black and blue data points in Fig. 7, especially in the range $D_{\rm L} \in \{20, 30\}$ Mpc. And similarly, a $\gtrsim 1\sigma$ shifts for lower values of $\Delta H_0/H_0$ when extending to farther distances. This redshift-dependent variation of the $0.2R_{\rm opt}$ bins' $\Delta H_0/H_0$ is also an indication of possible Malmquist-like bias and requires an in-depth assessment before including it in the joint analysis. This in turn is a clear indication that the innermost bin is in tension with the $\Delta H_0/H_0$ estimated using only the four conservative bins, implying that one should not straight away perform the joint analysis including the $0.2R_{\rm opt}$ bin and validates our original reasoning to exclude it from the main analysis. Indeed, we show the joint results here to highlight the differences and anticipate the implications for future investigations.

4.2 Smoothing the binned variance

While we have so far presented our results by binning the galaxies in distance, we now implement a simple smoothing of the scatter using the locally weighted scatter regression of the scatter (LOWESS[10]) obtained in the $\Delta H_0/H_0$ versus $D_{\rm L}$ plane. This technique has been utilized in various contexts in Montiel et al. (2014), Bernardo & Levi Said (2021), Escamilla-Rivera, Levi Said & Mifsud (2021) and Fernández-Hernández et al. (2019). We implement this essentially to represent the variation in $\Delta H_0/H_0$ as a smooth function of $D_{\rm L}$ and simultaneously obtain the uncertainty on the estimated variance. Similar to the binning schemes where we have to assume the size of the $\Delta D_{\rm L}$, here we need to assume a fraction ($f \in \{0, 1\}$) of the data that will be considered to obtain the locally weighted least squares fit. Higher values of this fraction will consider a larger number of data points eventually providing a smoother reconstruction of the scatter plot. This technique while being 'non-parametric' also allows one to obtain the uncertainty region by simply bootstrapping on the scatter points. We utilize this method to present our final constraints on the $\Delta H_0/H_0$ as our main result in terms of uncertainty and the upper limits.

We show the results of the LOWESS smoothing in Fig. 8 for three different scenarios: using only the central $0.6\,R_{\rm opt}$ bin alone, our baseline analysis with four radial bins and all six radial bins included. Here, we have utilized $f = 0.2$, while we have tested the results also with the larger fractions. We show a comparison of the constraints and 95 per cent upper limits on $\Delta H_0/H_0$ in Table 2, for $f = 0.2$ and 0.5 fractions. Using lower fractions ($f < 0.1$) tend to provide very few galaxies for each locally weighted regression, essentially mimicking the scatter with very large mean squared errors. Note that traditionally

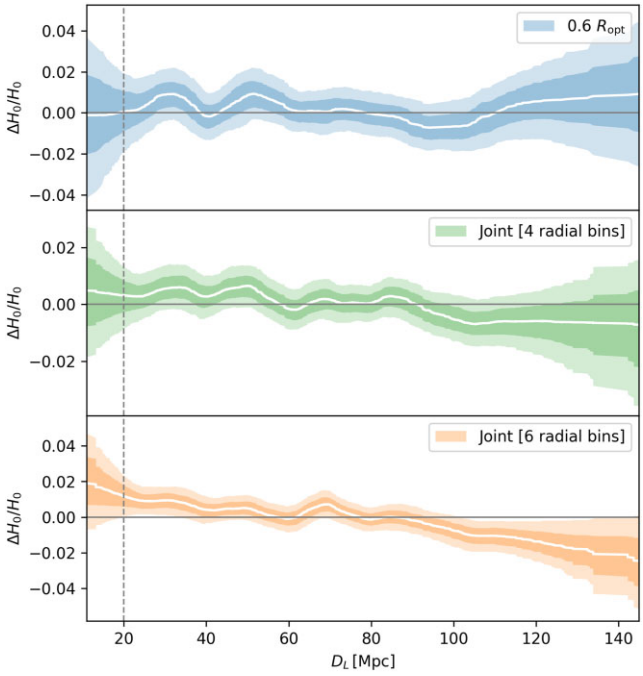

Figure 8. *Top*: We show the 1σ and 2σ C.L. of the fit to the $0.6R_{\rm opt}$ bin. *Centre*: Similar to the top panel, for the baseline joint analysis with the four radial bins and for comparison, we also show the results from all the six radial bins in the *Bottom* panel.

[10]Locally weighted scatter plot smoothing (LOWESS; Cleveland 1979; Cleveland & Devlin 1988). We utilize the publicly available `statsmodels` package Seabold & Perktold (2010) for this purpose. A simple example of how to perform the same can be found here. Please see also Cook & Weisberg (1999), Andersen (2009), and Fox (2024) for more details.

Table 2. We show the 95 % C.L. upper limits on the $\Delta H_0/H_0[\%]$, for the two cases of the fraction of data utilized in the analysis. The $f = 0.2$ column corresponds to the uncertainty regions presented in Fig. 8.

	$\Delta H_0/H_0[\%]$			
	$f = 0.2$		$f = 0.5$	
Bins	68 % C.L.	< 95 % C.L.	68 % C.L.	< 95 % C.L.
$0.6R_{\rm opt}$	$-0.11^{+2.06}_{-1.96}$	3.90	$0.35^{+1.04}_{-1.18}$	2.64
4 bins	$0.54^{+1.32}_{-1.37}$	2.98	$0.34^{+0.63}_{-0.74}$	1.74
6 bins	$2.08^{+1.65}_{-1.39}$	5.17	$1.45^{+0.72}_{-0.69}$	2.79

the fraction of data to be utilized is optimized for the least possible mean square error through cross-validation techniques (Montiel et al. 2014, see references therin). In our case, this typically corresponds to the larger values of f, as can be seen in the last column of Table 2. Therefore, we remain with the conservative $f = 0.2$ fraction of data to present the limits expected on $\Delta H_0/H_0$.

As shown in Table 2, using only the $0.6\,R_{\rm opt}$ bin, we find $\Delta H_0/H_0$ [per cent] $= -0.11^{+2.06}_{-1.96}$ with a 95 per cent C.L. upper limit of $\Delta H_0/H_0 < 3.9$ per cent. We interpret this limit as a conservative upper limit on the allowed local variation on H_0. Note that this limit is estimated at a distance $D_{\rm L} \sim 10$ [Mpc]. Similarly, we find the upper limit at 95 per cent C.L. limits is $\Delta H_0/H_0 \lesssim 3$ per cent, which we infer as our best estimate. It is worth noting that our estimates of $\Delta H_0/H_0(D_{\rm L})$ obtained from very local galaxies smoothed in distances are comparable to the local Hubble variance of $\sim$2 per cent H_0 reported in (Camarena & Marra 2018, see also Marra et al. (2013) and Wu & Huterer (2017)), albeit using a larger redshift range of $0.023 \leq z \leq 0.15$ in SNe data sets. Our results are in complete agreement with these studies and extend the arguments to more local distances. Needless to say, these limits are tighter when we utilize $f = 0.5$, as can be seen in the last two columns of Table 2. We also find that similar features are reconstructed in both these cases, validating the use of four bins as our baseline data set. We notice a mild dip at $D_{\rm L} \sim 100$ [Mpc] and a rise at $D_{\rm L} \sim 30$ [Mpc], albeit with a low significance of $\sim 1\sigma$. Finally, with the inclusion of the innermost radial bin, the redshift dependence of $\Delta H_0/H_0$ is evident as depicted in the bottom panel of Fig. 8. This also translates to a detection of $\Delta H_0/H_0 > 0$ at C.L. of $\sim 1\sigma (f = 0.2)$ and $\sim 2\sigma (f = 0.5)$.

4.3 Joint analysis

As anticipated in Section 3, we perform the joint analysis of the RTFs, considering the pivot point as a parameter of the fit and individual slopes and intrinsic scatters for each of the RTFs as free parameters. To validate this assumption, we first perform a rolling regression[11] analysis where no binning is considered but all the data points from all the bins are simultaneously fitted, assuming a gradually changing slope. Wherein we recover that all the regression lines pass through the pivot point without an explicit assumption of the same. In Fig. 2, we show the RTF relations fitted against data in this approach. As can be seen in Fig. 2 and also in Table 1, we find a very good agreement with the scenario when performing individual fits, especially contrasting the slope of the RTF relations. We obtain the following constraints for the pivot parameters

$$M_{\rm I}^{\rm Pivot} = -23.830 \pm 0.066,$$
$$\log_{10}(V^{\rm Pivot}) = 2.526 \pm 0.009.$$

The estimates of the intrinsic scatter and their uncertainty are at times lower than those obtained in the individual fits. This is clearly because a fraction of the uncertainty is now attributed to the estimation of the pivot and reduction in the overall degrees of freedom in the joint analysis. In Fig. C2, we show the correlations between the posteriors of the slopes and the pivot point. As expected, there exists a strong anticorrelation between the parameters $\log_{10}(V^{\rm Pivot})$ and $M_{\rm I}^{\rm Pivot}$. The slopes of the individual RTF relations are correlated with the coordinates of the pivot point, ranging from anticorrelations for the innermost $0.2R_{\rm opt}$ RTF to positive correlation for the outermost $1.2R_{\rm opt}$ RTF. In this context, it is interesting to note that the slope of $0.6R_{\rm opt}$ RTF is almost completely uncorrelated to the pivot point and shows only mild correlations with the slopes of the other RTFs. This also validates the existence of a very well-constrained individual RTF relation in this optical bin.

We show the complete contour plot of all the parameters of the MCMC analysis in Fig. C3, for brevity in the main text. The analysis so far has been performed assuming $H_0 = 70\,{\rm km\,s^{-1}\,Mpc^{-1}}$, which is necessary to estimate the distances to galaxies. In Fig. C1, we show the comparison, the posteriors when the H_0 is assumed differently, being either $67\,{\rm km\,s^{-1}\,Mpc^{-1}}$ Aghanim et al. (2020) or $73\,{\rm km\,s^{-1}\,Mpc^{-1}}$ Riess et al. (2021). As anticipated, the magnitude of the pivot point is strongly affected by the assumption, while the velocity remains completely unchanged. Also indicating that not assuming a particular value of H_0 mainly affects the overall scale of the RTF relations and not necessarily the shape of individual relations. However, the redshift dependence of the data can be affected by the assumption of underlying cosmology, and tentatively, this in turn can allow one to use the current data set to constrain the value of H_0. We intend to present this in the second instalment of this pilot analysis, utilizing also the necessary local distance calibrators.

4.4 Variance on the sky

As yet we have only estimated the variation of the Hubble parameter as a function of redshift; however, now we turn to the anisotropy in the estimate of the H_0 on the sky. For this purpose, we utilize the method presented in Soltis et al. (2019), wherein the angular clustering of the Supernovae sample Scolnic et al. (2018) and Riess et al. (2018a) was estimated and a per cent level spatial variation in the Hubble constant was reported. Following this methodology, we compute the spatial clustering of the galaxies in the current PSS95 sample, which is a collection of galaxies in the Southern hemisphere as shown in Fig. 4. Note, however, that in contrast to the SNe data sets that extend all the way to $z \lesssim 2.3$, our data set of local galaxies is restricted to $z \leq 0.03$, allowing us to test explicitly for the local anisotropy.

In Fig. 9, we show the power spectrum of the spatial clustering of the galaxies. The black data points and the associated uncertainties represent the clustering of the galaxies varying on the parameters of the RTF relations as fitted in the MCMC analysis Fig. C3. The blue-shaded region shows the 68 per cent C.L. uncertainty on the noise level associated with the statistical variation expected in an isotropic universe, given the observed positions of the current galaxies. As can be seen, the angular power spectrum of distribution of the galaxies in the current catalogue is perfectly consistent within the $\lesssim 1\sigma$ level, with the isotropic expectation, indicating no signal for anisotropy.

[11] We use `PyMC` Salvatier, Wiecki & Fonnesbeck (2016) and Wiecki (Wiecki 2021) for this purpose.

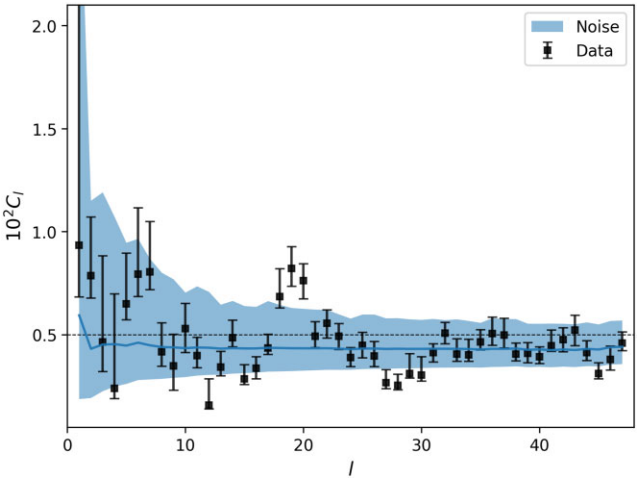

Figure 9. Power spectrum of the spatial clustering of the galaxies. The blue line shows the mean of the noise level, while the shaded region shows the 68 per cent C.L. uncertainty on the noise level.

The current sample only occupies the Southern hemisphere, which is reflected in the data and the noise level as large values of the angular power spectrum for $l = 1, 2$ and is completely consistent with what is expected. Also, note that the uncertainty in the data shown as the error bars in Fig. 9, only takes into account the variation of parameters of the RTFs and a fixed $H_0 = 70\,\mathrm{km\,s^{-1}\,Mpc^{-1}}$. We do not anticipate that the values of H_0 (also q_0) or so any variation in cosmology would affect distances to all the galaxies almost equivalently unless neglecting the redshift dependence in the current redshift range. Therefore, a full assessment can be warranted when H_0 is utilized as a free parameter alongside the local distance calibrators to obtain more quantitative limits on the level of isotropy. This, however, is not expected to change the inference here that the current galaxy sample is completely consistent with the null hypothesis of isotropy.

In the current analysis, we have refrained from doing further quantitative analysis to estimate the anisotropic variation of H_0. However, it is instructive to extend the data set to farther redshifts and larger sky coverage to be able to compare with studies of anisotropies in SNe samples (Soltis et al. 2019; Krishnan et al. 2022; Zhai & Percival 2022; Mc Conville & Colgáin 2023) and galaxy cluster analyses (Migkas et al. 2021, for example). In Zhai & Percival (2022) (and also in Mc Conville & Colgáin (2023)), a maximum angular variation of $\sim 4\,\mathrm{km\,s^{-1}\,Mpc^{-1}}$ was observed in different hemispheres of the sky. This shall also be immensely important to compare against the evidence of large-scale bulk flows reported in Watkins et al. (2023) and possible alignments with direction-dependent spatial variations observed in CMB analysis (Fosalba & Gaztanaga 2021; Yeung & Chu 2022) and it's correlation with local observables (Mc Conville & Colgáin 2023).

5 CONCLUSIONS AND OUTLOOK

We have presented the usefulness of the astrophysical scaling relation, in particular, the RTF Yegorova & Salucci (2007), to assess the variation in the Hubble parameter in the local Universe. While similar studies have been performed using the TF relation earlier, here we use RTF for the very first time. This empirical relation exploits the information of the full RC rather than one single reference value, as done using the TF relation. From a physical point of view, in contrast to the TF relation, the RTF takes into account the presence of DM in galaxies and the variation in them of the stellar mass-to-light ratios. The primary results of our analysis are summarized as follows:

(i) We constrain the maximum possible variance in the Hubble parameter as a function of redshift in the range of $0.005 < z < 0.035$ to be $\Delta H_0/H_0 \lesssim 3$ per cent at 95 per cent C.L., showing no significant redshift dependence.

(ii) Conservatively, using only the $0.6R_{\rm opt}$ radial bin, we find the consistent with our baseline analysis using four radial bins with $\Delta H_0/H_0 \lesssim 4$ per cent at 95 per cent, estimated at $D_{\rm L} \sim 10$ [Mpc].

(iii) These constraints allow us to conservatively conclude that any local solutions to alleviate the H_0-tension are not supported within the redshift range of the current galaxy sample.

(iv) We introduce a joint analysis of the 'independent' RTF relations, reducing the number of parameters while assessing the possible correlation between them. This also provides us with a possible pseudo-standardization of the RTFs.

(v) While occupying only the Southern hemisphere, spatial clustering of the current galaxies shows no deviation from the null hypothesis of isotropy.

Constraining the value of the present expansion rate (H_0) is one of the most crucial aspects of the current cosmological crisis. Exploring different independent methods and possible synergies in these data sets will yield a better understanding of changing the current cosmological paradigm in a more consistent direction. Needless to say, it is important to validate the analysis with newer/larger data sets and to assess the same in higher redshift ranges and with larger complete sky coverage to assess the spatial variations of H_0 (Migkas et al. 2021; Zhai & Percival 2022; Mc Conville & Colgáin 2023). In this context, we intend to extend the current analysis to much larger samples of galaxies, like PROBES (Stone et al. 2022) and MANGA (Arora et al. 2021), also accessing farther redshifts (Sharma et al. 2021; Sharma, Salucci & van de Ven 2022) to provide a comprehensive understanding of the evolution of the local and late Universe. This is also necessary to validate the possible alternative inference when the innermost radial bin $0.2\,R_{\rm opt}$ is included in the joint analysis, which indicates a variation of $\Delta H_0/H_0 \sim 10$ per cent, which is sufficiently apt to explain the H_0-tension.

On the other hand, as a second instalment to this pilot study, we intend to perform a joint analysis utilizing the local distance estimators (Riess et al. 2021) to calibrate the RTFs and constrain the value H_0. To this end, we have introduced here the joint analysis of the RTFs that will be a preliminary step in this direction, allowing a pseudo-standardization of the empirical RTF relations.

ACKNOWLEDGEMENTS

The authors are grateful to Leandros Perivolaropoulos, Stephane Courteau, Anto I. Lonappan, Nikhil Arora, and Konstantinos Migkas for useful comments on the draft and insightful discussions. BSH is supported by the INFN INDARK grant.

DATA AVAILABILITY

The data products utilized in the manuscript are all publicly available and appropriately referenced. The code utilized to perform the analysis here can be made available on reasonable request soon after acceptance of the paper.

REFERENCES

Abdalla E. et al., 2022, JHEAp, 34, 49
Addison G. E., Watts D. J., Bennett C. L., Halpern M., Hinshaw G., Weiland J. L., 2018, ApJ, 853, 119
Adil S. A., Akarsu O., Di Valentino E., Nunes R. C., Özülker E., Sen A. A., Specogna E., 2024, Phys. Rev. D, 109, 023527
Aghanim N. et al., 2020, A&A, 641, A6
Akarsu O., Barrow J. D., Escamilla L. A., Vazquez J. A., 2020, Phys. Rev. D, 101, 063528
Akarsu O., Colgáin E. O., Sen A. A., Sheikh-Jabbari M. M., 2024, preprint (arXiv:2402.04767)
Akarsu O., Di Valentino E., Kumar S., Nunes R. C., Vazquez J. A., Yadav A., 2023
Alam S. et al., 2021, Phys. Rev. D, 103, 083533
Alestas G., Camarena D., Di Valentino E., Kazantzidis L., Marra V., Nesseris S., Perivolaropoulos L., 2022, Phys. Rev. D, 105, 063538
Alestas G., Kazantzidis L., Perivolaropoulos L., 2021, Phys. Rev. D, 103, 083517
Anchordoqui L. A., 2021, Phys. Rev. D, 103, 035025
Andersen R., 2009, Annu. Rev. Sociol., 35, 67
Andrade U., Bengaly C. A. P., Alcaniz J. S., Capozziello S., 2019, MNRAS, 490, 4481
Andrade U., Bengaly C. A. P., Santos B., Alcaniz J. S., 2018, ApJ, 865, 119
Arora N., Stone C., Courteau S., Jarrett T. H., 2021, MNRAS, 505, 3135
Banerjee S., Petronikolou M., N. Saridakis E., 2023, PoS, CORFU2022, 263
Bargiacchi G., Dainotti M. G., Capozziello S., 2023b, MNRAS, 525, 3104
Bargiacchi G., Dainotti M. G., Nagataki S., Capozziello S., 2023a, MNRAS, 521, 3909
Benevento G., Hu W., Raveri M., 2020, Phys. Rev. D, 101, 103517
Benisty D., 2023, PoS, CORFU2022, 259
Bernal J. L., Verde L., Jimenez R., Kamionkowski M., Valcin D., Wandelt B. D., 2021, Phys. Rev. D, 103, 103533
Bernardo R. C., Levi Said J., 2021, JCAP, 08, 027
Blakeslee J. P., Jensen J. B., Ma C.-P., Milne P. A., Greene J. E., 2021, ApJ, 911, 65
Blinov N., Keith C., Hooper D., 2020, JCAP, 2020, 005
Bonvin V. et al., 2017, MNRAS, 465, 4914
Cai R.-G., Ding J.-F., Guo Z.-K., Wang S.-J., Yu W.-W., 2020, Phys. Rev. D., 103, 123539
Camarena D., Marra V., 2018, Phys. Rev. D, 98, 023537
Camarena D., Marra V., 2019, MNRAS, 495, 2630
Camarena D., Marra V., 2023, preprint (arXiv:2307.02434)
Cao S., Ratra B., 2023, Phys. Rev. D, 107, 103521
Castello S., Högås M., Mörtsell E., 2022, JCAP, 07, 003
Chen G. C. F. et al., 2019, MNRAS, 490, 1743
Cleveland W. S., 1979, J. Am. Stat. Assoc., 74, 829
Cleveland W. S., Devlin S. J., 1988, J. Am. Stat. Assoc., 83, 596
Colgáin E. Ó., Van Putten M. H. P. M., Yavartanoo H., 2019, Phys. Lett. B., 793, 126
Cook R. D., Weisberg S., 1999, Applied Regression Including Computing and Graphics. John Wiley & Sons, Ltd, Chichester, England, UK, https://onlinelibrary.wiley.com/doi/book/10.1002/9780470316948
Courteau S., 1997, AJ, 114, 2402
Dainotti M. G., Bargiacchi G., Bogdan M., Lenart A. L., Iwasaki K., Capozziello S., Zhang B., Fraija N., 2023, ApJ, 951, 63
Dainotti M. G., De Simone B., Schiavone T., Montani G., Rinaldi E., Lambiase G., 2021, ApJ, 912, 150
Dainotti M. G., De Simone B., Schiavone T., Montani G., Rinaldi E., Lambiase G., Bogdan M., Ugale S., 2022, Galaxies, 10, 24
de Jaeger T., Stahl B. E., Zheng W., Filippenko A. V., Riess A. G., Galbany L., 2020, MNRAS, 496, 3402
de la Macorra A., Almaraz E., Garrido J., 2022, Phys. Rev. D, 105, 023526
Desmond H., Jain B., Sakstein J., 2019, Phys. Rev. D, 100, 043537
Desmond H., Sakstein J., 2020, Phys. Rev. D, 102, 023007
Di Paolo C., Salucci P., Fontaine J. P., 2019, ApJ, 873, 106
Di Valentino E. et al., 2021, Astropart. Phys., 131, 102605
du Mas des Bourboux H. et al., 2020, ApJ, 901, 153
Du S.-S., Wei J.-J., You Z.-Q., Chen Z.-C., Zhu Z.-H., Liang E.-W., 2023, MNRAS, 521, 4963
Efstathiou G., 2020, preprint(arXiv:2007.10716)
Escamilla-Rivera C., Levi Said J., Mifsud J., 2021, JCAP, 2021, 016
Fernández-Hernández L. M., Montiel A., Rodríguez-Meza M. A., 2019, MNRAS, 488, 5127
Fontaine J.-P. et al., 2018, in 53rd Rencontres de Moriond on Cosmology. ARISF, Paris, p. 363
Foreman-Mackey D., Hogg D. W., Lang D., Goodman J., 2013, PASP, 125, 306
Fosalba P., Gaztanaga E., 2020, MNRAS, 504, 5840
Fox J., 2024, Applied Regression Analysis and Generalized Linear Models, SAGE Publications, https://us.sagepub.com/en-us/nam/applied-regression-analysis-and-generalized-linear-models/book237254
Freedman W. L. et al., 2019, ApJ, 882, 34
Freedman W. L., 2021, ApJ, 919, 16
Gómez-Valent A., 2018, JCAP, 05, 026
Gómez-Valent A., Favale A., Migliaccio M., Sen A. A., 2024, Phys. Rev. D, 109, 023525
Haridasu B. S., Luković V. V., Moresco M., Vittorio N., 2018, JCAP, 10, 015
Haridasu B. S., Viel M., 2020, MNRAS, 497, 1757
Haridasu B. S., Viel M., Vittorio N., 2021, Phys. Rev. D, 103, 063539
Högås M., Mörtsell E., 2023, Phys. Rev. D, 108, 124050
Hoscheit B. L., Barger A. J., 2018, Astrophys. J., 854, 46
Hu J.-P., Wang F.-Y., 2023, Universe, 9, 94
Huang C. D. et al., 2020, ApJ, 889, 5
Jedamzik K., Pogosian L., Zhao G.-B., 2021, Commun. in Phys., 4, 123
Jee I., Suyu S., Komatsu E., Fassnacht C. D., Hilbert S., Koopmans L. V. E., 2019, Science, 365, 1134
Karukes E. V., Salucci P., 2017, MNRAS, 465, 4703
Karwal T., Kamionkowski M., 2016, Phys. Rev., D94, 103523
Keenan R. C., Barger A. J., Cowie L. L., 2013, ApJ, 775, 62
Kenworthy W. D., Scolnic D., Riess A., 2019, ApJ, 875, 145
Khosravi N., Baghram S., Afshordi N., Altamirano N., 2019, Phys. Rev., D99, 103526
Knox L., Millea M., 2020, Phys. Rev. D, 101, 043533
Kourkchi E., Tully R. B., Anand G. S., Courtois H. M., Dupuy A., Neill J. D., Rizzi L., Seibert M., 2020, ApJ, 896, 3
Kourkchi E., Tully R. B., Courtois H. M., Dupuy A., Guinet D., 2022, MNRAS, 511, 6160
Kreisch C. D., Cyr-Racine F.-Y., Doré O., 2020, Phys. Rev. D, 101, 123505
Krishnan C., Colgáin E. O., Sheikh-Jabbari M. M., Yang T., 2021, Phys. Rev. D, 103, 103509
Krishnan C., Mohayaee R., Colgáin E. O., Sheikh-Jabbari M. M., Yin L., 2022, Phys. Rev. D, 105, 063514
Lapi A., Boco L., Cueli M. M., Haridasu B. S., Ronconi T., Baccigalupi C., Danese L., 2023, ApJ, 959, 83
Lee N., Ali-Haïmoud Y., Schöneberg N., Poulin V., 2023, Phys. Rev. Lett., 130, 161003
Lemos P., Lee E., Efstathiou G., Gratton S., 2019, MNRAS, 483, 4803
Lenart A. L., Bargiacchi G., Dainotti M. G., Nagataki S., Capozziello S., 2023, ApJS, 264, 46
Lewis A., 2019, preprint (arXiv:1910.13970)
Li X., Liao K., 2024, Astrophys. J., 966, 121
Liao K., Shafieloo A., Keeley R. E., Linder E. V., 2020, ApJ, 895, L29
Liu Y., Yu H., Wu P., 2023, ApJ, 946, L49
Luković V. V., Haridasu B. S., Vittorio N., 2018, Found. Phys., 48, 1446
Luković V. V., Haridasu B. S., Vittorio N., 2019, MNRAS, 491, 2075
Lyu M.-Z., Haridasu B. S., Viel M., Xia J.-Q., 2020, ApJ, 900, 160
Marra V., Amendola L., Sawicki I., Valkenburg W., 2013, Phys. Rev. Lett., 110, 241305
Marra V., Perivolaropoulos L., 2021, Phys. Rev. D, 104, L021303
Mathewson D. S., Ford V. L., Buchhorn M., 1992, ApJS, 81, 413
Mc Conville R., Colgáin E. O., 2023, Phys. Rev. D, 108, 123533
McGaugh S. S., 2005, ApJ, 632, 859
McGaugh S. S., Schombert J. M., Bothun G. D., de Blok W. J. G., 2000, ApJ, 533, L99

Migkas K., Pacaud F., Schellenberger G., Erler J., Nguyen-Dang N. T., Reiprich T. H., Ramos-Ceja M. E., Lovisari L., 2021, A&A, 649, A151
Montiel A., Lazkoz R., Sendra I., Escamilla-Rivera C., Salzano V., 2014, Phys. Rev. D, 89, 043007
Mortsell E., Goobar A., Johansson J., Dhawan S., 2021, Astrophys. J., 933, 212
Mortsell E., Goobar A., Johansson J., Dhawan S., 2022, ApJ, 935, 58
Niedermann F., Sloth M. S., 2021a, Phys. Rev. D, 103, L041303
Niedermann F., Sloth M. S., 2021b, Phys. Rev. D, 103, 103537
Nygaard A., Holm E. B., Tram T., Hannestad S., 2023, preprint (arXiv:2307.00418)
Pandey S., Raveri M., Jain B., 2020, Phys. Rev. D, 102, 023505
Perivolaropoulos L., Skara F., 2022, New Astron. Rev., 95, 101659
Perivolaropoulos L., Skara F., 2023, MNRAS, 520, 5110
Persic M., Salucci P., Stel F., 1996, MNRAS, 281, 27
Pesce D. W. et al., 2020, ApJ, 891, L1
Poulin V., 2020, in 3rd World Summit on Exploring the Dark Side of the Universe. p. 17
Poulin V., Smith T. L., Bartlett A., 2021, Phys. Rev. D., 104, 123550
Qi J.-Z., Meng P., Zhang J.-F., Zhang X., 2023, Phys. Rev. D, 108, 063522
Riess A. G. et al., 2016, ApJ, 826, 56
Riess A. G. et al., 2018a, ApJ, 853, 126
Riess A. G. et al., 2018b, ApJ, 855, 136
Riess A. G. et al., 2024, Astrophys. J. Lett., 962, L17
Riess A. G., 2019, Nature Rev. Phys., 2, 10
Riess A. G., Casertano S., Yuan W., Bowers J. B., Macri L., Zinn J. C., Scolnic D., 2021, ApJ, 908, L6
Roy Choudhury S., Hannestad S., Tram T., 2021, JCAP, 03, 084
Ruchika, Rathore H., Roy Choudhury S., Rentala V., 2024, JCAP, 06, 056
Salucci P., 2008, IAU Symp., 244, 53
Salucci P., 2019, Astron. Astrophys. Rev., 27, 2
Salucci P., Burkert A., 2000, ApJ, 537, L9
Salucci P., Frenk C. S., Persic M., 1993, MNRAS, 262, 392
Salucci P., Ratnam C., Monaco P., Danese L., 2000, MNRAS, 317, 488
Salvatier J., Wiecki T. V., Fonnesbeck C., 2016, PeerJ Comput. Sci., 2, e55
Schombert J., McGaugh S., Lelli F., 2020, AJ, 160, 71
Schöneberg N., Franco Abellán G., Pérez Sánchez A., Witte S. J., Poulin V., Lesgourgues J., 2022, Phys. Rept., 984, 1
Scolnic D. M. et al., 2018, ApJ, 859, 101
Seabold S., Perktold J., 2010, in 9th Python in Science Conference, p. 92
Shah P., Lemos P., Lahav O., 2021, Astron. Astrophys. Rev., 29, 9
Shajib A. J. et al., 2020, MNRAS, 494, 6072
Shanks T., Hogarth L. M., Metcalfe N., 2019, MNRAS, 484, L64
Sharma G., Salucci P., Harrison C. M., van de Ven G., Lapi A., 2021, MNRAS, 503, 1753
Sharma G., Salucci P., van de Ven G., 2022, A&A, 659, A40
Silva C., 2023, preprint (arXiv:2312.05267)
Solà J., Gómez-Valent A., de Cruz Pérez J., 2017, Phys. Lett. B, 774, 317
Soltis J., Farahi A., Huterer D., Liberato C. M., 2019, Phys. Rev. Lett., 122, 091301
Stone C., Courteau S., Arora N., Frosst M., Jarrett T. H., 2022, ApJS, 262, 33
Tarnopolski M., 2017, MNRAS, 472, 4819
Tristram M. et al., 2024, Astron. Astrophys., 682, A37
Tully R. B., 2023, preprint (arXiv:2305.11950)
Tully R. B., Fisher J. R., 1977, A&A, 54, 661
Tutusaus I., Kunz M., Favre L., 2023, preprint (arXiv:2311.16862)
Tutusaus I., Lamine B., Blanchard A., 2019, A&A, 625, A15
Vagnozzi S., 2020, Phys. Rev. D, 102, 023518
Vagnozzi S., 2023, Universe, 9, 393
Vattis K., Koushiappas S. M., Loeb A., 2019, Phys. Rev. D, 99, 121302
Verde L., Schöneberg N., Gil-Marín H., 2023, preprint (arXiv:2311.13305)
Verde L., Treu T., Riess A. G., 2019, Nature Astron., 3, 891
Vogt N. P., Haynes M. P., Giovanelli R., Herter T., 2004, AJ, 127, 3325
Watkins R. et al., 2023, MNRAS, 524, 1885
Whitbourn J. R., Shanks T., 2014, MNRAS, 437, 2146
Wiecki T., 2021 , in Team P. ed., PyMC examples
Wojtak R., Hjorth J., 2022, MNRAS, 515, 2790
Wojtak R., Hjorth J., 2024, preprint (arXiv:2403.10388)
Wojtak R., Hjorth J., Hjortlund J. O., 2023, MNRAS, 525, 5187
Wong K. C. et al., 2020, MNRAS, 498, 1420
Wu H.-Y., Huterer D., 2017, MNRAS, 471, 4946
Yegorova I. A., Salucci P., 2007, MNRAS, 377, 507
Yeung S., Chu M.-C., 2022, Phys. Rev. D, 105, 083508
Yuan W., Riess A. G., Macri L. M., Casertano S., Scolnic D., 2019, ApJ, 886, 61
Zhai Z., Percival W. J., 2022, Phys. Rev. D, 106, 103527
Zhao G.-B. et al., 2019, MNRAS, 482, 3497
Zhao M.-M., He D.-Z., Zhang J.-F., Zhang X., 2017, Phys. Rev., D96, 043520

APPENDIX A: DERIAVTION OF THE VARIANCE

As shown in Section 3, the distance modulus, which is written as equation (7) can be utilized to estimate the magnitude fluctuation by differentiating it on either side at a given redshift treating data as constant and assuming variation only in the physical parameters absolute magnitude ($M_{\rm I}$) and the Hubble parameter (H_0) as,

$$\mathrm{d}M = \mathrm{d}(5\log_{10}(V_{\rm rec}/H_0)) \equiv \frac{5}{\log 10}\frac{\mathrm{d}H_0}{H_0} \tag{A1}$$

which when discretized in redshift can be written as equation (12). Wherein L.H.S can be estimated straightaway from the distribution of residuals in the RFT diagram $M_{\rm I}$ vs. $\log_{10}(V)$ (see Fig. 2) at a given redshift translating to the fractional variation in H_0. The same can be achieved simply by writing the differential variation in $M \rightarrow M + \Delta M$ and $H_0 \rightarrow H_0 + \Delta H_0$ in equation (7) and performing Taylor expansion. Please see Luković, Haridasu & Vittorio (2018) and Wu & Huterer 2017 (eq. 4 therin) for a detailed discussion, however, in the context of supernovae magnitudes.

APPENDIX B: ALTERNATE BINNING OF THE DISTANCE

In the main text, we have presented our primary results using a bin size of $\Delta D_{\rm L} = 20$ [Mpc], using linear binning of the magnitude residuals. In this section, we briefly report the mild differences we notice when different binning schemes are utilized. In Fig. B1, we show the $\Delta H_0/H_0$ using a logarithmic binning scheme. We notice that the joint constraint shows a mild jump in the mean value of $\Delta H_0/H_0$ towards lower redshifts in the closest distance bin, although with no strong significance. And while being completely consistent

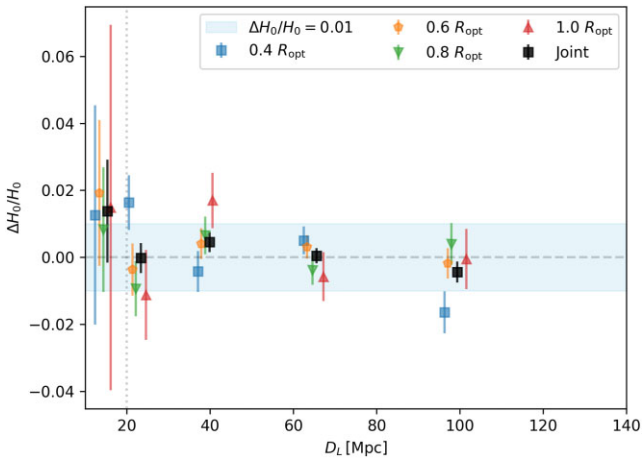

Figure B1. Same as Fig. 6 for the logarithmic binning of distance as described in Appendix B.

with $\Delta H_0/H_0 = 0$ for distances larger than 20 [Mpc]. Note that this is particularly interesting in the context of some of the ultra late-time resolutions to H_0-tension, as we mentioned in the main text. The closet distance bins centred at $\sim$15 [Mpc] and $\sim$23 [Mpc] contain about 10, 100 galaxies in each, respectively. The most local distance bin, with very few galaxies, seems to consistently suggest a mild jump in H_0, even for our conservative $0.6R_{\rm opt}$ bin. This, as we have already mentioned in the main text, is more evident when the innermost $0.2\ R_{\rm opt}$ bin is included in the joint analysis.

APPENDIX C: CONTOUR PLOTS OF THE JOINT ANALYSIS

For the sake of brevity in the main text, we show the contour plots of the joint analysis here. As elaborated in the main text, we can see that the slopes of the individual RTFs are correlated to a certain extent in the joint analysis, while the intrinsic scatters of the same have negligible correlation. Also, one can notice that the intrinsic scatter of the bin $\sigma_n(0.6\,\mathrm{Ropt})$ almost shows lower intrinsic scatter, validating that this radial bin is well constrained. Similarly, also the slope $a_n(0.6\,\mathrm{Ropt})$ can be seen to have negligible correlation with the rest of the RTFs slopes.

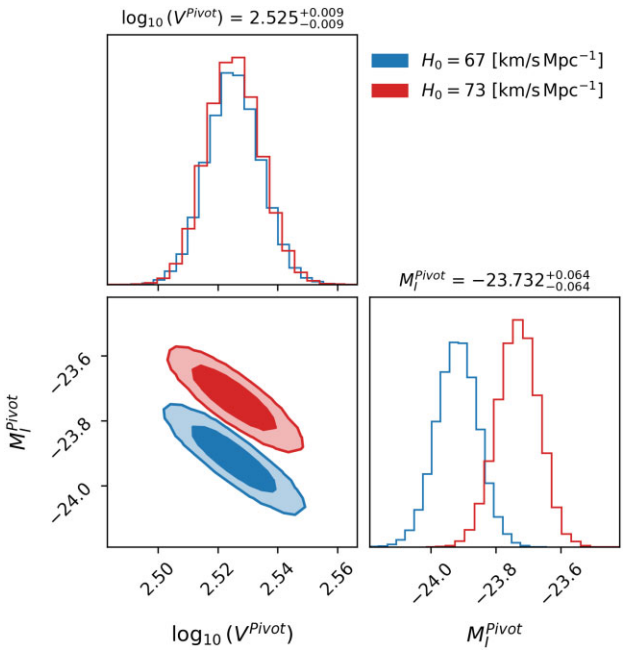

Figure C1. We show the 68 and 95 per cent C.L. posteriors for the parameters $\log_{10}(V^{\rm Pivot})$ and $M_{\rm I}^{\rm Pivot}$, when the likelihood analysis is performed assuming $H_0 = 67\,\mathrm{km\,s^{-1}\,Mpc^{-1}}$ (blue) and $H_0 = 73\,\mathrm{km\,s^{-1}\,Mpc^{-1}}$ (red). The 1σ parameter constraints for the case of $H_0 = 73\,\mathrm{km\,s^{-1}\,Mpc^{-1}}$ are shown on top of the 1D posteriors.

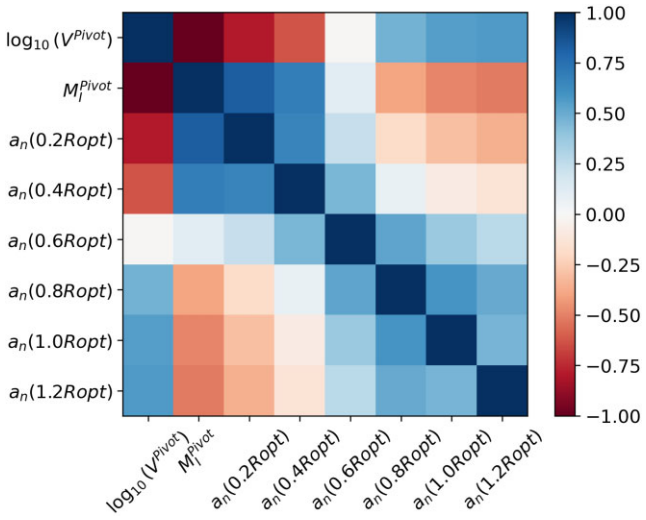

Figure C2. Correlation between the posteriors of the estimated slopes for the individual RTF relations and the pivot point.

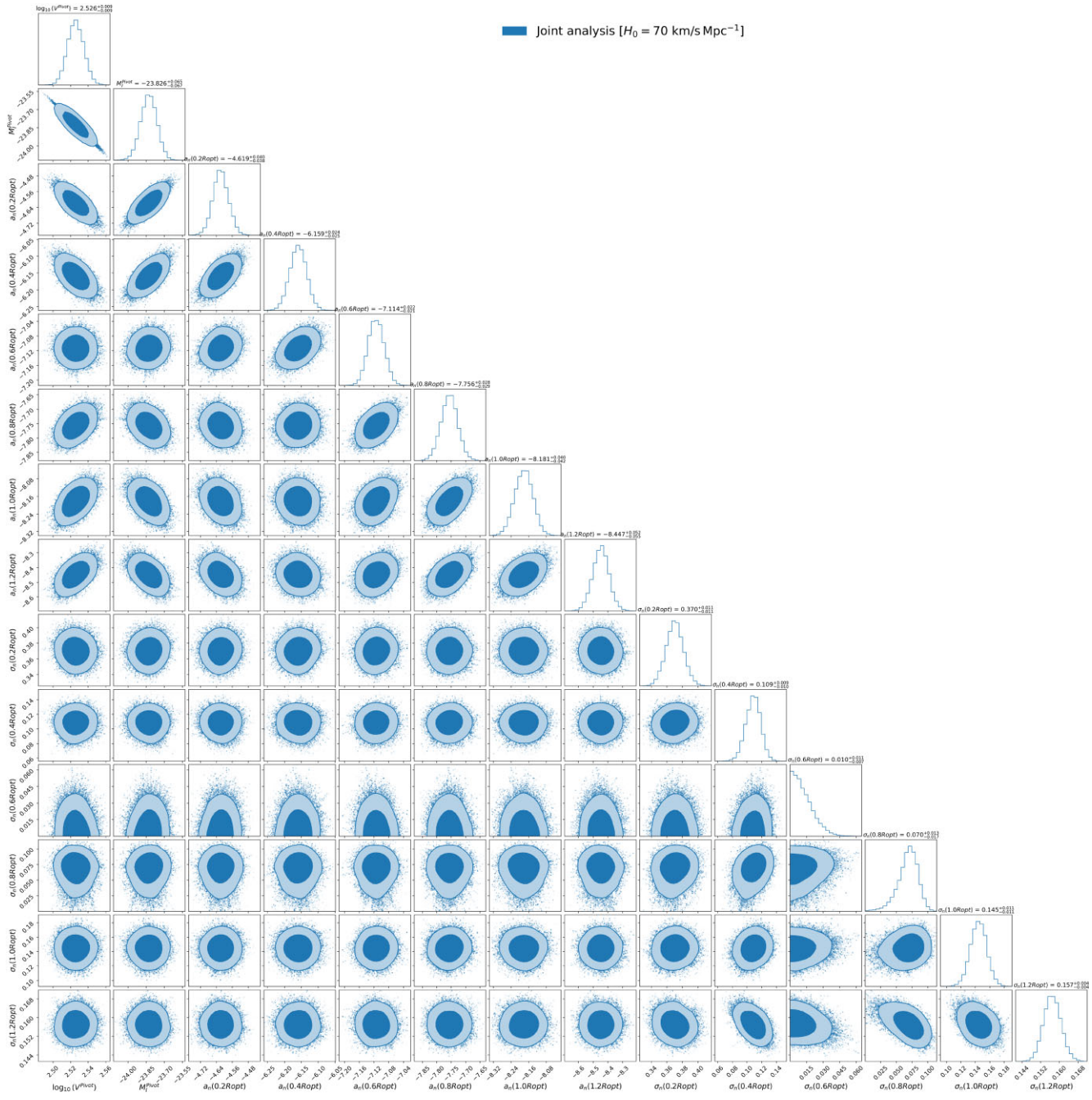

Figure C3. Contour plots showing the 68 and 95 per cent C.L. for all the parameters in the joint analysis of the RTFs. We assume the $H_0 = 70\,\mathrm{km\,s^{-1}\,Mpc^{-1}}$.

This paper has been typeset from a TEX/LATEX file prepared by the author.